Uniaxial magnetic anisotropy and anomalous Hall effect in the ferromagnetic compound PrMn₂Ge₂

Xiao-Yan Wang, Sheng Xu, Huan Wang, Jun-Fa Lin, Xiang-Yu Zeng, Xiao-Ping Ma, Jing Gong, Yi-Ting Wang,
Kun Han, and Tian-Long Xia ●*

Department of Physics, Renmin University of China, Beijing 100872, P. R. China
and Beijing Key Laboratory of Opto-electronic Functional Materials & Micro-nano Devices,
Renmin University of China, Beijing 100872, P. R. China

Noncolinear or noncoplanar spin configurations in magnetic materials usually give rise to a fascinating array of physical phenomena. Here, we perform a systematic study of magnetic and electronic transport properties in a noncolinear itinerant magnet PrMn₂Ge₂. With the field applied along different directions, PrMn₂Ge₂ displays uniaxial magnetic anisotropy with an easy axis along the c axis. Both the temperature-dependent magnetization and longitudinal resistivity reveal an anomaly at 330 K, well corresponding to the magnetic transition of the Mn sublattice from a colinear antiferromagnetic state to a canted ferromagnetic state. Strikingly, PrMn₂Ge₂ exhibits anomalous Hall effect (AHE) together with prominent negative magnetoresistivity (MR) when the field is applied along the c axis. The negative MR can be linked to the suppression of spin scattering. Based on the scaling analysis between the anomalous Hall resistivity ρ_{yx}^A and longitudinal resistivity ρ_{xx}, the relationship $\rho_{yx}^A \propto \rho_{xx}^{1.18}$ has been given, which indicates that the observed AHE in PrMn₂Ge₂ is likely dominated by the skew-scattering mechanism. Simultaneously, a sharp jump has been observed in the hysteresis loop, which is also discernible in the field dependence of Hall resistivity and magnetoresistivity. Such features presumably result from the movement of the domain wall.

I. INTRODUCTION

Skyrmions or skyrmion bubbles-hosting materials have attracted immense interest in condensed matter physics for promising applications in spintronic devices [1–4]. Thus far, various intriguing phenomena associated with the nontrivial spin textures, including the topological Hall effect [5,6], skyrmion Hall effect [7,8], skyrmion magnetic resonance [9], etc., have been identified. These stirring properties, coupled with the steady particlelike nature, tiny size, and topological stability, highlight skyrmions as potential information carriers in memory devices [2–4]. However, the experimentally detected magnetic skyrmions or skyrmion bubbles usually exist at low temperatures [10] and less is observed near room temperature. From the viewpoint of better practical applications, further exploration on other physics properties pertaining to reported systems with unique room-temperature skyrmion or skyrmion bubbles is therefore indispensable.

Prominently, the rare earth-transition metal compounds REMn₂Ge₂ (RE = rare-earth element) have been recently reported as a unique system hosting stabilized magnetic skyrmion bubbles near room temperature [11,12]. Materials in this family usually crystallize in a body-centered-tetragonal structure of ThCr₂Si₂-type with the space group $I4/mmm$. The RE, Mn, and Ge layers are arranged alternately along the c axis following the sequence of -RE-Ge-Mn-Ge-RE- [13,14]. In regard to the magnetic properties, both the rare earth and manganese sublattice play a significant role in these compounds. In general, the magnetic order in the manganese sublattice persists up to temperatures higher than 300 K, whereas the rare earth sublattice only exhibits magnetic order at low temperatures. A diversity of spin configurations have been proposed and verified in these compounds based on theory and experiments [15–17]. Besides, recent attention has also focused on them due to their anomalous Hall effect (AHE) [18,19] and noncoplanar spin textures-induced topological Hall effect (THE) [12,18–21]. All the observations mentioned above remind us that these compounds merit further investigation.

PrMn₂Ge₂, falling into the family of REMn₂Ge₂, possesses intricate magnetic structures depending on temperature as reported in substantial works [22–24]. Briefly, PrMn₂Ge₂ undergoes a transition from the paramagnetic state (PM) to a colinear antiferromagnetic (AFM) state with the Mn moments lying in the intralayers at the Néel temperature T_N up to 415 K, termed as AFl type magnetic structure, then enters into a canted ferromagnetic (FM) state with a commensurate intralayer antiferromagnetic component (Fmc type) at $T_{c1} \sim 330$ K, the canting angle with the c axis is about 65°. As temperature drops more to $T_{c2} \sim 280$ K, PrMn₂Ge₂ converts to a conical ferromagnetic state with an incommensurate intralayer antiferromagnetic component (Fmi type). The cone semiangle is approximately 58° from the c axis and the interlayer component of moments remains ferromagnetic along the c direction. It should be noticed that such a Fmi type magnetic structure in the Mn sublattice persists to the lowest temperature. On further cooling of PrMn₂Ge₂ to ~ 40 K (T_c^{Pr}), magnetic order occurs in the Pr sublattice, which couples ferromagnetically with the ferromagnetic component of the

conical Mn spins along the c axis. Although extensive works have been reported to investigate the magnetic properties of $PrMn_2Ge_2$, the study on electronic transport properties is currently absent, which would provide an inherent and deeper knowledge of $PrMn_2Ge_2$.

In this study, we synthesized high-quality single crystals of $PrMn_2Ge_2$ and implemented a comprehensive study of its magnetic and electronic transport properties. The uni-axial magnetic anisotropy with an easy axis along the c axis has been observed as the field is applied in different directions. $PrMn_2Ge_2$ shows significant negative magnetore-sistivity (MR) with the field applied along the c axis, which is ascribed to the suppression of spin scattering. Strikingly, we found an AHE with an approximately linear relationship between the anomalous Hall resistivity ρ_{yx}^A and longitudinal resistivity ρ_{xx}, namely $\rho_{yx}^A \propto \rho_{xx}^{1.18}$, indicating the obtained AHE might be described by the skew scattering mechanism. Furthermore, a conspicuous jump, likely produced by the motion of the domain wall, has been observed in the hysteresis loop, as well as in the field dependence of Hall resistivity and magnetoresistivity, which awaits further check with magnetic force microscopy.

II. EXPERIMENTAL DETAILS

Single crystals of $PrMn_2Ge_2$ were prepared via the indium flux method. Pr ingots, Mn powder, Ge powder, and In pieces were loaded into an alumina crucible with a molar ratio of Pr : Mn : Ge : In = 1 : 2 : 2 : 30 before being sealed in an evacuated quartz tube. The tube was then heated to 1100 °C, dwelled there for 20 h, and finally cooled down to 700 °C with the rate of 3 °C / h. Platelike single crystals were dissociated from the flux with a centrifuge at this temperature. Chemical compositions of the single-crystal $PrMn_2Ge_2$ were confirmed to be Pr : Mn : Ge = 1 : 2 : 2 by using energy dispersive X-ray spectroscopy (EDX, Oxford X-Max 50). The single-crystal X-ray diffraction (XRD) and powder XRD data were collected with a Brucker D8 Advance X-ray diffractometer using Cu K_α radiation. TOPAS-4.2 was employed for the refinement.

The measurements of magnetic properties were carried out on the Quantum Design magnetic property measurement system (QD MPMS-3). The longitudinal resistivity ρ_{xx} and Hall resistivity ρ_{yx} were measured using a standard six-probe method on the Quantum Design physical property measurement system (QD PPMS-14T). To eliminate the influence of the voltage probe misalignment, the raw data of ρ_{xx} and ρ_{yx} were gathered under both negative (sweeping the field from 0 T to −5 T) and positive field (sweeping the field from 0 T to 5 T). Then the total ρ_{xx} and ρ_{yx} are assessed using the formula $\rho_{xx}(B) = [\rho_{xx}(+B) + \rho_{xx}(-B)]/2$ and $\rho_{yx}(B) = [\rho_{yx}(+B) + \rho_{yx}(-B)]/2$, respectively. B is related to the extra magnetic field ($\mu_0 H$) by $B = \mu_0[H + (1 − N_d)M)]$, where N_d is the demagnetization factor, μ_0 is the vacuum permeability, and M is the magnetization. All the experiments are conducted on the same rectangular sample.

III. RESULTS AND DISCUSSIONS

As depicted in Fig. 1(a), $PrMn_2Ge_2$ crystallizes in a centrosymmetric tetragonal structure. The Pr, Mn, and Ge layers
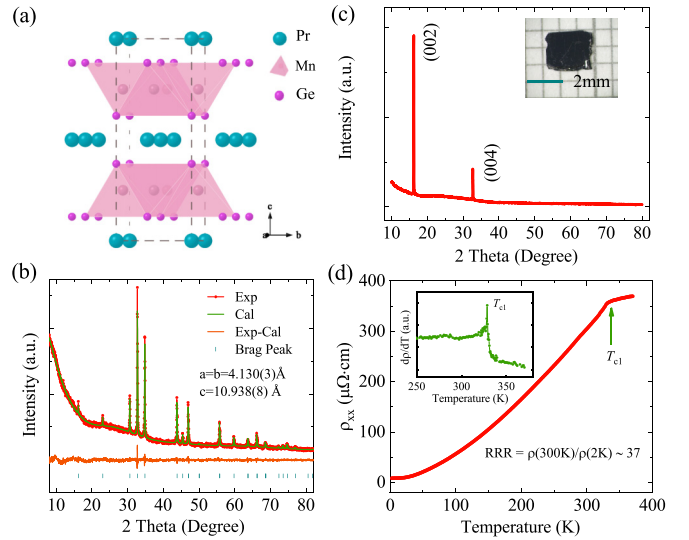

FIG. 1. (a) Sketch of $PrMn_2Ge_2$ Crystal structure. (b) Rietveld refined powder XRD patterns of crushed sample. (c) The single-crystal XRD pattern of $PrMn_2Ge_2$, the inset shows a photograph of the as-grown single crystal. (d) The longitudinal resistivity as a function of temperature at zero field. The T_{c1} is marked as green arrow. The inset shows the curve of $d\rho_{xx}/dT$-T.

are arranged alternately along the c axis in the sequence of -Pr-Ge-Mn-Ge-Pr-. Figure 1(b) displays the powder XRD patterns of crushed single crystals. All the peaks can be finely refined with space group $I4/mmm$ (No. 139). The refined lattice parameters are $a = b = 4.130(3)$ Å, $c = 10.938(8)$ Å, in coincidence with previously reported values [13,14]. The interlayer Mn-Mn distance is determined by $c/2 = 5.469(4)$ Å, which is slightly greater than the nearest intralayer Mn-Mn distance calculated by $a/\sqrt{2} = 2.920(1)$ Å. Figure 1(c) presents the single-crystal XRD pattern. The sharp peaks are well indexed as the (00l), indicating the naturally cleaved surface is the ab plane. A photograph of typical single-crystal $PrMn_2Ge_2$ is shown in the inset of Fig. 1(c). Temperature (T) dependence of longitudinal resistivity $\rho_{xx}(T)$, as presented in Fig. 1(d), demonstrates a metallic behavior over the entire temperature range. The sizable value of residual resistivity ratio (RRR) estimated by ρ_{xx} (300 K) / ρ_{xx} (2 K) is 37, indicating that the as-grown sample is of high quality. A distinct kink has been observed above room temperature, marked as the Curie temperature T_{c1}, which well corresponds to the magnetic transition from AFl type to Fmc type. The T_{c1} is 330 K, further determined by the peak position of the $d\rho_{xx}/dT$ vs T curve as presented in the inset of Fig. 1(d). Furthermore, a faster decrease of longitudinal resistivity below T_{c1} is observed, which is attributed to the reduction of spin disorder-induced scattering.

Temperature dependence of magnetization $M(T)$ for $PrMn_2Ge_2$ were plotted in Figs. 2(a) and 2(b) with the magnetic field applied parallel to the c axis ($B \parallel c$) and ab plane ($B \parallel ab$), respectively. For both directions, zero-field-cooled (ZFC) and field-cooled (FC) magnetization curves show sharp upturns at high temperature, consistent with the FM transition of Mn sublattice as mentioned above. This is more obvious in the derivative dM/dT curves in the insets of Figs. 2(a)
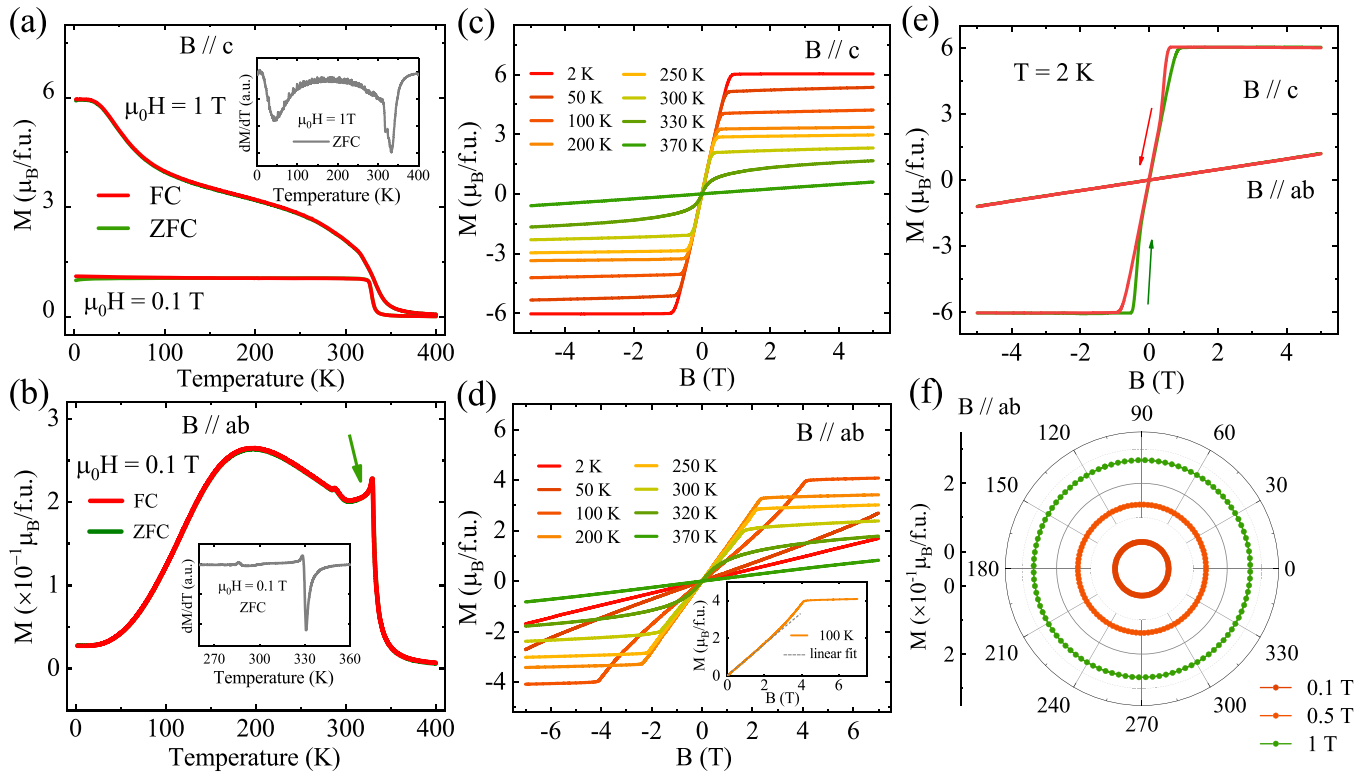
FIG. 2. Temperature dependence of magnetization in the ZFC and FC modes under several fields (a) for $B \parallel c$ and (b) for $B \parallel ab$. The insets indicate the corresponding dM/dT-T curves. A jump just below T_{c1} is marked as the green arrow in (b). (c) and (d) The magnetization as a function of magnetic field at different temperatures for $B \parallel c$ and $B \parallel ab$. The inset of (d) shows the isothermal magnetization at 100 K, which exhibits a nonlinear increase with the increasing field before saturation. The dashed line is the linear fit. (e) The comparison of magnetization at 2 K between the case of $B \parallel c$ and $B \parallel ab$. The red solid lines represent the measurement process with the field sweeping from 5 T to -5 T whereas the green solid lines mean the field sweeps from -5 T to 5 T, which has also been marked with the red and green arrows, respectively. (f) The angular dependence of magnetization under several fields at 10 K.

and 2(b), where clear peaks have been observed at the characteristic temperature $T_{c1} = 330$ K for both cases, in agreement with the T_{c1} estimated from the ρ_{xx}-T curve. Regarding the case of $H \parallel c$, the data shows slight ZFC-FC splitting at low temperature as a field of $\mu_0 H = 0.1$ T is applied, which is mainly due to the formation of FM domains. Besides, evidence of the FM order from the Pr sublattice is obtained from a further increase of magnetization at 36 K with the applied field of 1 T. On the contrary, when the field is applied parallel to the ab plane, except for the well displayed FM transition at T_{c1}, another kink has been observed in the M-T curve around 280 K, which is in line with the transition of magnetic structure from Fmc type to Fmi type at T_{c2}. Note that there is a sudden jump just below T_{c1}. Such a feature, termed as magnetic anomaly in $Fe_{5-x}GeTe_2$ [25], is widely accepted as the onset of the magnetic soliton lattice in helimagnets, which has been theoretically and experimentally validated [26–28]. The possibility of a magnetic soliton lattice in $PrMn_2Ge_2$ will be later simply argued with the data of M-B curves. Upon further cooling T, the magnetization shows a distinct drop at low temperature, as evident in Fig. 2(b), which is primarily attributed to the AFM ground state in the ab plane.

The magnetization of $PrMn_2Ge_2$ is displayed as a function of magnetic field in Fig. 2(c) for $B \parallel c$. For simplicity, the data presented here is collected by sweeping the field from 0 T to 5 T and 0 T to -5 T, the same procedure as the aforementioned

longitudinal resistivity and Hall resistivity measurements. All curves below T_{c1} show a linear increase with the increasing field and finally approach saturation, which suggests a typical FM behavior. At 2 K, the saturated magnetization M_s reaches $6.04 \, \mu_B/\text{f.u.}$ (μ_B and f.u. stand for the Bohr magneton and formula unit, respectively) under B ~ 0.89 T, which is in fair agreement with the previous reported value ($M_s = 5.90 \, \mu_B/\text{f.u.}$) in single-crystal $PrMn_2Ge_2$ [29], whereas the field-dependent magnetization results in distinctly different behaviors in the case of $B \parallel ab$, as displayed in Fig. 2(d). Particularly, the curves gathered at low temperatures exhibit a nonlinear behavior before saturation, which can be observed obviously from the isothermal magnetization for 100 K in the inset of Fig. 2(d). In fact, such nonlinear increase on the field-dependent magnetization has been properly discussed as a scenario of magnetic soliton lattice formation theoretically [30] and generally observed in some systems with helical magnetic structure [26,31], whose magnetic soliton lattice was directly presented by Lorentz microscopy [28]. As for $PrMn_2Ge_2$, a helical spin structure along the c axis can arise from the ab-plane component of its conical ferromagnetic structure [23], which may continuously evolve into a magnetic soliton lattice phase with a field perpendicular to the helical axis based on the well-established theory [30]. Accordingly, the nonlinear behavior observed here in $PrMn_2Ge_2$ just with $B \parallel ab$, coinciding well with the magnetic structure
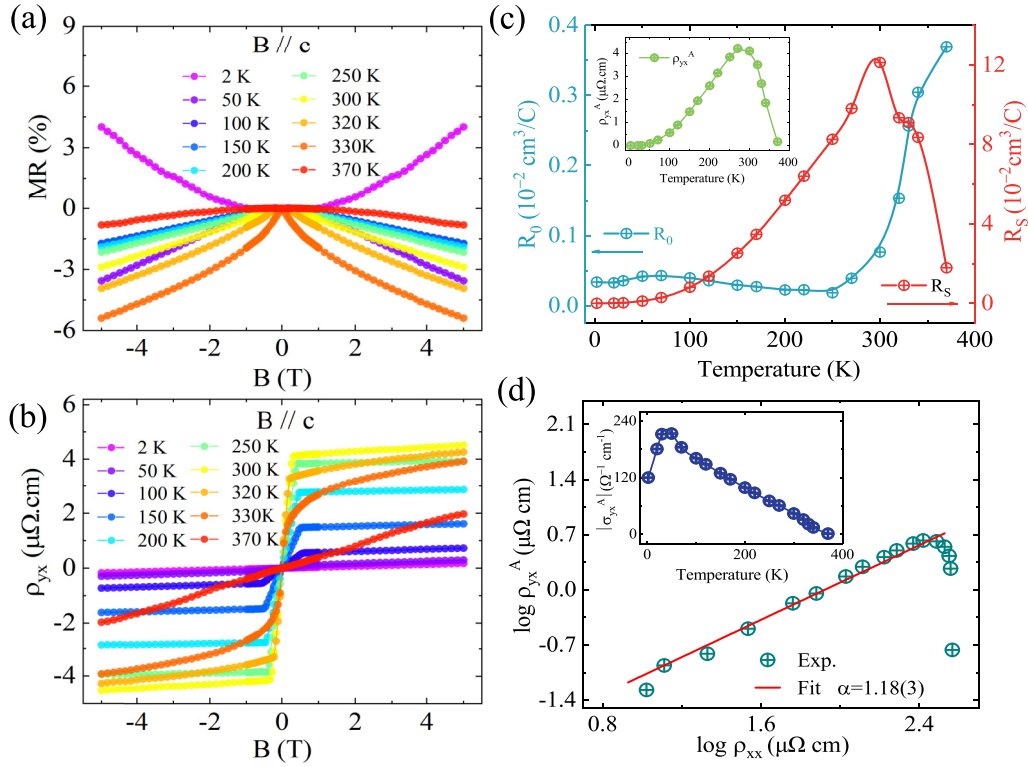
FIG. 3. Field dependence of (a) magnetoresistivity and (b) Hall resistivity at different temperatures for $B \parallel c$ and $I \parallel a$. (c) The normal Hall coefficient R_0 and anomalous Hall coefficient R_S as a function of temperature. The inset of (c) presents the temperature dependence of anomalous Hall resistivity. (d) The plot of $\log \rho_{yx}^A$ versus $\log \rho_{xx}$. The red solid line is the fit with the scaling law $\rho_{xy}^A \propto \rho_{xx}^\alpha$. Inset shows the anomalous Hall conductivity as a function of temperature.

of PrMn$_2$Ge$_2$, likely stems from the formation of a magnetic soliton lattice. Besides, the saturated magnetization is approximately $4.11 \mu_B$/f.u. at 100 K and gradually increases with the decreasing temperature in both cases of $B \parallel c$ and $B \parallel ab$. In other words, the same saturated magnetization at 2 K for $B \parallel ab$ is anticipated as that for $B \parallel c$ as long as a higher field is applied. For clarity, Fig. 2(e) presents the comparison of magnetization loop at 2 K between the case of $B \parallel c$ and $B \parallel ab$. A prominent hysteresis is observed for $B \parallel c$ but not for $B \parallel ab$, suggesting that there are FM components of moments along the c axis. An abnormal shape of hysteresis loop has also been noticed, which will be discussed in detail later. Note that no saturation signal of the magnetization is observed for $B \parallel ab$, even the field strengths up to 7 T in Fig. 2(d). Furthermore, the angular dependence of magnetization with the field rotating in the ab plane is presented in Fig. 2(f). The data reveals an almost isotropic behavior in the ab plane, which is expected from the proposed magnetic structure. Despite such complexity of magnetism as mentioned above, it is apparent that PrMn$_2$Ge$_2$ possesses uniaxial magnetic anisotropy and the easy magnetization axis is the c axis within the entire temperature range, which is evident from M-B and M-T curves in different directions.

Next, we turn to characterize the electronic transport properties of PrMn$_2$Ge$_2$. The field dependence of longitudinal resistivity $\rho_{xx}(B)$, together with the field-dependent Hall resistivity $\rho_{yx}(B)$ measurement, was carried out with $B \parallel c$ and the electric current (I) parallel to the a axis ($I \parallel a$). The magnetoresistivity (MR), defined as MR =

$[\rho_{xx}(B) - \rho_{xx}(0)]/\rho_{xx}(0) \times 100\%$, is plotted in Fig. 3(a). It is clearly shown that the signs of MR are opposite in the case of low and high temperature. At high temperature, negative MR with a maximum value of 5.7% at $T_{c1} = 330$ K (B = 5 T) has been observed, which is owing to the suppression of spin scattering with an extra field as commonly reported in ferromagnetic systems. In contrast, the sign of MR is switched from negative to positive with reducing temperature, which reveals that the conventional MR, generated by Lorentz force-induced spiral motion of the conduction electrons, dominates at low temperature.

The Hall resistivity ρ_{yx} as a function of magnetic field for different temperatures is plotted in Fig. 3(b), which exhibits a linear field dependence for $T > T_{c1}$. Instead, the curves show two distinct regions below T_{c1}. In the low-field region, the Hall resistivity increases sharply with an increase in field. While it becomes nearly field-independent in the high-field region. Obviously, the $\rho_{yx}(B)$ curves highly resemble the trend of $M(B)$ curves at corresponding temperatures, confirming the presence of anomalous Hall effect in the target single crystal. It should be pointed out that no additional signal is observed on both MR and ρ_{yx} curves within the temperature range of 240–320 K and the low-magnetic field region of 40–70 mT, where the skymion bubbles exist for polycrystalline REMn$_2$Ge$_2$ [11]. Generally, the measured Hall resistivity in a ferromagnetic system is composed of two terms [32], i.e., $\rho_{yx} = \rho_{yx}^N + \rho_{yx}^A = R_0 B + R_S \mu_0 M$, where ρ_{yx}^N is the normal Hall resistivity related to Lorentz effect and ρ_{yx}^A is the anomalous Hall resistivity. R_0 and R_S represent the normal and
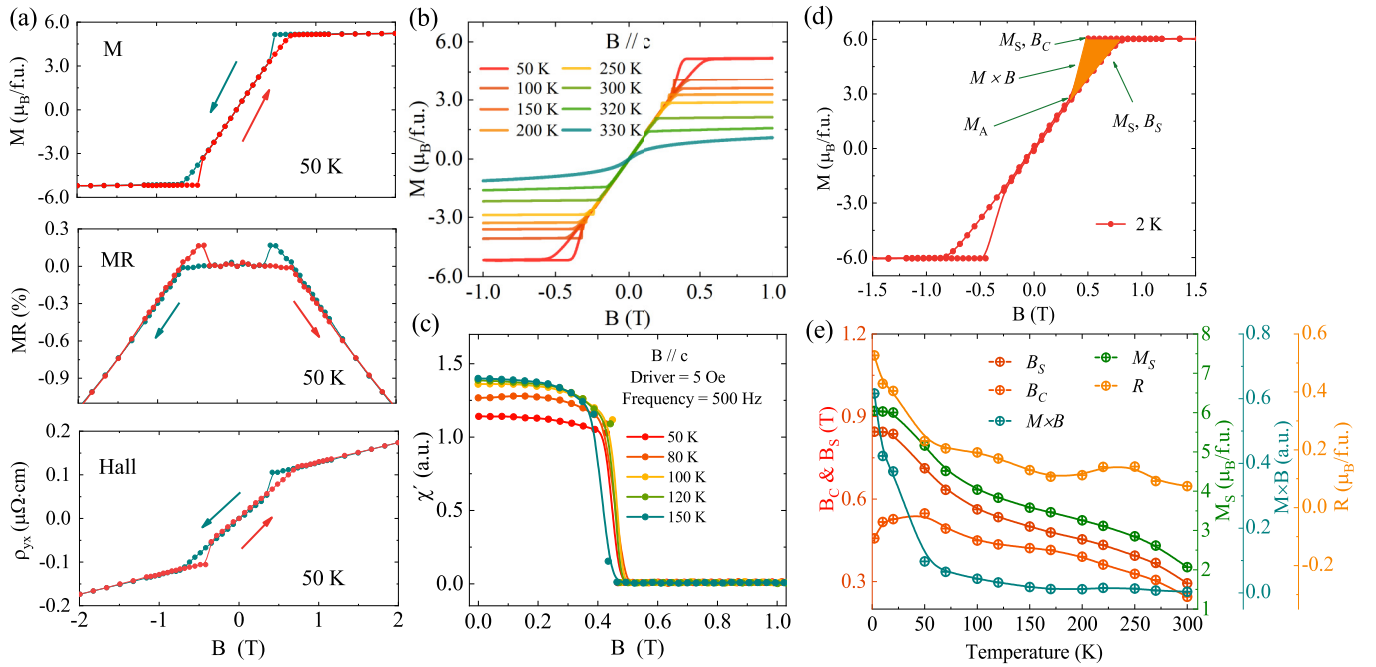
FIG. 4. (a) The field dependence of magnetization, magnetoresistivity, and Hall resistivity taken with the same experimental procedure at 50 K for $B \parallel c$. The red lines represent the measurement process with the field sweeping from -5 T to 5 T whereas the dark cyan lines mean the field sweeps from 5 T to -5 T. (b) The hysteresis loop with abnormal drops at different temperatures. (c) The real part of the field-dependent ac susceptibility. (d) The hysteresis loop at 2 K. The parameters including M_S, B_S, B_C, M_A, and $M \times B$ are defined as indicated by arrows. (e) The temperature dependence of different parameters.

anomalous Hall coefficient, respectively. Accordingly, the values of R_0 and ρ_{yx}^A can be estimated from the linear fit of $\rho_{yx}(B)$ in the high-field region. The slope and intercept correspond to the R_0 and ρ_{yx}^A, respectively. R_S is then derived utilizing the formula $\rho_{yx}^A = R_S \mu_0 M_S$. The obtained results are presented in Fig. 3(c). Over the entire measured temperature range, R_0 is positive, indicating the majority carriers are holes. The carrier concentration (n) is further estimated by $n = 1/ \mid e R_0 \mid$, which reaches 1.8×10^{22} cm^{-3} at 2 K. Both ρ_{yx}^A and R_S increase as the temperature increases with a prominent maximum at 300 K, a temperature slightly below $T_{c1} (\sim 0.9\ T_{c1})$. Such a feature has already been reported in Fe$_3$GeTe$_2$ single crystals [33] and Mn$_5$Ge$_3$ thin films [34].

It is well recognized that anomalous Hall effect can arise from three mechanisms, namely the skewing scattering, side jump, and Berry curvature-related intrinsic mechanism [35]. To explore the possible origin of the AHE observed in PrMn$_2$Ge$_2$, the anomalous Hall conductivity (σ_{yx}^A) is calculated using the formula $\sigma_{yx}^A = |\rho_{yx}^A/(\rho_{yx}^2 + \rho_{xx}^2)|$. The temperature dependence of (σ_{yx}^A) with a maximum of 220 Ω^{-1}cm^{-1} is plotted in the inset of Fig. 3(d). In theory, the Berry curvature-related term generally gives rise to a large intrinsic anomalous Hall conductivity ($\sigma_{yx,in}^A$) in the order of $e^2/(hc)$, where e, h, and c are the electronic charge, Plank constant, and lattice parameter, respectively [36]. Using the lattice parameter $c = 10.938(8)$ Å, the anticipated $\sigma_{yx,in}^A$ in PrMn$_2$Ge$_2$ is 353 Ω^{-1}cm^{-1}, larger than the experimentally measured value. In contrast, the contribution of a side-jump mechanism can be expressed as $[e^2/(hc)](\varepsilon_{so}/E_F)$, where ε_{so} is the energy of spin-orbit interaction and E_F is the Fermi

energy [37]. Since the value of ε_{so}/E_F is generally less than 0.01 for metallic ferromagnets, the side-jump mechanism induced σ_{yx}^A is commonly much smaller than $\sigma_{yx,in}^A$ and the observed value in PrMn$_2$Ge$_2$. Hence, the dominant mechanism of the AHE should be further ascertained. Based on the well-established theory, the exponent α determined by the scaling law $\rho_{xy}^A \propto \rho_{xx}^\alpha$ is also a characteristic parameter to check which mechanism generates the AHE [35]. More precisely, $\alpha = 1$ refers to the AHE that results from the skew scattering mechanism, while $\alpha = 2$ refers to the AHE that results from the intrinsic or side jump mechanisms. Accordingly, scaling analysis between $\log \rho_{yx}^A$ and $\log \rho_{xx}$ has been employed in Fig. 3(d). The exponent α equals 1.18, which suggests that the AHE might be dominated by the skew scattering mechanism.

As mentioned above, the magnetization shows a sharp drop as H decreases from high field, bringing out two tiny triangles in the $M(B)$ loop. It is surprising that such a drop has also been discernible in the curves of $\rho_{yx}(B)$ and MR taken with the same experimental procedure, as presented in Fig. 4(a), indicating that the magnetism and electronic transport properties are intimately related. Figure 4(b) exhibits the hysteresis loop at several temperatures, which decreases gradually as the temperature increases and finally disappears above $T > T_{c1}$. Note that the drops occur in a tiny field range of 0.003 T and finally disappear when temperature approaches T_{c1}. The specific shape of hysteresis loop, persisting in a broad temperature range over a wide temperature range below T_{c1} in PrMn$_2$Ge$_2$, have been also reported in moloclinic Cr$_5$Te$_8$ [38], TbMn$_6$Sn$_6$ [39], and BaFe$_{12}$O$_{19}$ [40]. Particularly in BaFe$_{12}$O$_{19}$, such an anomaly has been exhaustively studied using magnetic force microscopy and attributed to the motion

of domain wall. To further explore the feature in $PrMn_2Ge_2$, the measurement of *ac* susceptibility is carried out at different temperatures below T_{c1}. The results have been demonstrated in Fig. 4(c). All curves show distinct drops around 0.5 T, in agreement with the value extracted from $M(B)$ curves as discussed below. For clarity, several relevant parameters including M_S, B_S, B_C, M_A, and $M \times B$ have been defined. When the field gradually increases, the magnetization reaches saturation at a critical field. Here the field is defined as B_S, the saturated magnetization is M_S as mentioned before. B_C is another critical field where the sharp drop occurs when the field decreases from high field. The magnetization at this time is numerically equal to M_S and the magnetization after the drop is defined as M_A. $M \times B$ stands for the hysteresis loss, which is estimated by the area of the yellow triangle displayed in Fig. 4(d). To further assess the degree of change in magnetization before and after the jump, the mutation ratio $R = (M_S - M_A)/M_S$ is assessed based on the above parameters. The obtained parameters are plotted as a function of temperature in Fig. 4(e). It is clear that B_S, M_S, and $M \times B$ exhibit the same temperature dependence. They all increase with the decreasing temperature as expected in the systems with FM coupling due to an enhanced magnetic exchange at low temperatures. All the extracted values of B_C are close to 0.5 T with a slight increase when the temperature decreases. It indicates that there is a mutation of domain wall at 0.5 T as investigated in an early report [40]. It has been noticed that there is a drop in B_C at low temperature, which might be attributed to the influence of Pr spins. At the same time, the R reveals a maximum value of 0.5 (50%) at 2 K. It should be mentioned that measurements on different samples have been conducted to check the reliability of the phenomenon mentioned above. Here, we have reported such phenomena from the view of magnetic transport. While the precise process of the field-induced domain wall movement in $PrMn_2Ge_2$ has so far remained elusive, which is expected to be further checked on magnetic force microscopy.

IV. CONCLUSIONS

In this work, we synthesized high-quality single crystals of $PrMn_2Ge_2$, which exhibit abundant magnetic structures that vary with temperature. The magnetization curves clearly indicate three magnetic transitions over the temperature range of 2 K–400 K. With the field applied in different directions, the uniaxial magnetic anistropy has been observed and the easy magnetization axis is parallel to the *c* axis. Then the comprehensive electronic properties of $PrMn_2Ge_2$ have been investigated. Strikingly, the AHE together with prominent negative MR is observed as the field is applied along the *c* axis. The negative MR is commonly entangled with the suppression of spin scattering under an extra field. Possible origination of the observed AHE in $PrMn_2Ge_2$ is discussed. In particular, an approximately linear scaling between the anomalous Hall resistivity and longitudinal resistivity reveals that the AHE in $PrMn_2Ge_2$ is dominated by the skew scattering mechanism. Besides, the hysteresis loop exhibits an abnormal jump, which is also obvious in the field dependence of ρ_{yx} and MR loops. Such an anomaly might be caused by the motion of the domain wall. However, the precise process of the domain wall movement remains unclear in $PrMn_2Ge_2$, which is of interest to further check based on magnetic force microscopy. To sum up, our results enrich the properties of magnetic materials with noncolinear spin textures, especially the system of skyrmion bubbles, which holds a promising application in future memory devices.

[1] T. H. R. Skyrme, Nucl. Phys. **31**, 556 (1962).

[2] A. Fert, V. Cros, and J. Sampaio, Nat. Nanotechnol. **8**, 152 (2013).

[3] N. Nagaosa and Y. Tokura, Nat. Nanotechnol. **8**, 899 (2013).

[4] K. Yamada, S. Kasai, Y. Nakatani, K. Kobayashi, H. Kohno, A. Thiaville, and T. Ono, Nat. Mater. **6**, 270 (2007).

[5] A. Neubauer, C. Pfleiderer, B. Binz, A. Rosch, R. Ritz, P. G. Niklowitz, and P. Böni, Phys. Rev. Lett. **102**, 186602 (2009).

[6] N. Kanazawa, Y. Onose, T. Arima, D. Okuyama, K. Ohoyama, S. Wakimoto, K. Kakurai, S. Ishiwata, and Y. Tokura, Phys. Rev. Lett. **106**, 156603 (2011).

[7] G. Chen, Nat. Phys. **13**, 112 (2017).

[8] W. Jiang, X. Zhang, G. Yu, W. Zhang, X. Wang, M. Benjamin Jungfleisch, J. E. Pearson, X. Cheng, O. Heinonen, K. L. Wang *et al.*, Nat. Phys. **13**, 162 (2017).

[9] Y. Onose, Y. Okamura, S. Seki, S. Ishiwata, and Y. Tokura, Phys. Rev. Lett. **109**, 037603 (2012).

[10] Z. Ma and L. Li, Phys. Status Solidi A **219**, 2100333 (2022).

[11] Z. Hou, L. Li, C. Liu, X. Gao, Z. Ma, G. Zhou, Y. Peng, M. Yan, X.-x. Zhang, and J. Liu, Mater. Today Phys. **17**, 100341 (2021).

[12] S. Wang, Q. Zeng, D. Liu, H. Zhang, L. Ma, G. Xu, Y. Liang, Z. Zhang, H. Wu, R. Che *et al.*, ACS Appl. Mater. Interfaces **12**, 24125 (2020).

[13] K. Narasimhan, V. Rao, R. Bergner, and W. Wallace, J. Appl. Phys. **46**, 4957 (1975).

[14] R. Welter, G. Venturini, E. Ressouche, and B. Malaman, J. Alloys Compd. **218**, 204 (1995).

[15] I. Nowik, Y. Levi, I. Felner, and E. Bauminger, J. Magn. Magn. Mater. **147**, 373 (1995).

[16] A. Szytuła and J. Leciejewicz, Handbook on the physics and chemistry of rare earths **12**, 133 (1989).

[17] N. Kolmakova, A. Sidorenko, and R. Levitin, Low Temp. Phys. **28**, 653 (2002).

[18] G. Gong, L. Xu, Y. Bai, Y. Wang, S. Yuan, Y. Liu, and Z. Tian, Phys. Rev. Mater. **5**, 034405 (2021).

[19] L. Xu, Y. Bai, G. Gong, F. Song, Z. Li, Y. Han, L. Ling, and Z. Tian, Phys. Rev. B **105**, 075108 (2022).

[20] X. Zheng, X. Zhao, J. Qi, X. Luo, S. Ma, C. Chen, H. Zeng, G. Yu, N. Fang, S. U. Rehman *et al.*, Appl. Phys. Lett. **118**, 072402 (2021).

[21] G. Xu, D. Liu, L. He, S. Wang, and L. Ma, Mater. Lett. **315**, 131963 (2022).

[22] S. Kervan, A. Kilic, and A. Gencer, J. Phys.: Condens. Matter **16**, 4955 (2004).

[23] S. Kennedy, J. Wang, S. Campbell, M. Hofmann, and S. Dou, J. Appl. Phys. **115**, 172617 (2014).

[24] M. Song, J. Zhao, C. Liu, M. He, Y. Wang, Y. Han, L. Ling, L. Cao, L. Zhang, Z. Qu *et al.*, Appl. Phys. Lett. **120**, 092402 (2022).

[25] T. T. Ly, J. Park, K. Kim, H.-B. Ahn, N. J. Lee, K. Kim, T.-E. Park, G. Duvjir, N. H. Lam, K. Jang *et al.*, Adv. Funct. Mater. **31**, 2009758 (2021).

[26] Y. Kousaka, Y. Nakao, J.-i. Kishine, M. Akita, K. Inoue, and J. Akimitsu, Nucl. Instrum. Methods Phys. Res., Sect. A **600**, 250 (2009).

[27] J.-i. Kishine, K. Inoue, and Y. Yoshida, Prog. Theor. Phys. Suppl. **159**, 82 (2005).

[28] Y. Togawa, T. Koyama, K. Takayanagi, S. Mori, Y. Kousaka, J. Akimitsu, S. Nishihara, K. Inoue, A. Ovchinnikov, and J.-i. Kishine, Phys. Rev. Lett. **108**, 107202 (2012).

[29] N. Iwata, T. Ikeda, T. Shigeoka, H. Fujii, and T. Okamoto, J. Magn. Magn. Mater. **54-57**, 481 (1986).

[30] J.-i. Kishine and A. Ovchinnikov, Solid State Phys. **66**, 1 (2015).

[31] Y. Cao, Z. Huang, Y. Yin, H. Xie, B. Liu, W. Wang, C. Zhu, D. Mandrus, L. Wang, and W. Huang, Mater. Today Adv. **7**, 100080 (2020).

[32] C. Hurd, *The Hall Effect in Metals and Alloys* (Springer Science & Business Media, 2012).

[33] Y. Wang, C. Xian, J. Wang, B. Liu, L. Ling, L. Zhang, L. Cao, Z. Qu, and Y. Xiong, Phys. Rev. B **96**, 134428 (2017).

[34] C. Zeng, Y. Yao, Q. Niu, and H. H. Weitering, Phys. Rev. Lett. **96**, 037204 (2006).

[35] N. Nagaosa, J. Sinova, S. Onoda, A. H. MacDonald, and N. P. Ong, Rev. Mod. Phys. **82**, 1539 (2010).

[36] S. Onoda, N. Sugimoto, and N. Nagaosa, Phys. Rev. Lett. **97**, 126602 (2006).

[37] P. Nozieres and C. Lewiner, J. Phys. France **34**, 901 (1973).

[38] Z. Z. Jiang, X. Luo, J. Yan, J. J. Gao, W. Wang, G. C. Zhao, Y. Sun, J. G. Si, W. J. Lu, P. Tong, X. B. Zhu, W. H. Song, and Y. P. Sun, Phys. Rev. B **102**, 144433 (2020).

[39] H. Zhang, J. Koo, C. Xu, M. Sretenovic, B. Yan, and X. Ke, Nat. Commun. **13**, 1091 (2022).

[40] Z. Yang, M. Lange, A. Volodin, R. Szymczak, and V. V. Moshchalkov, Nat. Mater. **3**, 793 (2004).